

Dalton Transactions

Accepted Manuscript



This is an *Accepted Manuscript*, which has been through the Royal Society of Chemistry peer review process and has been accepted for publication.

Accepted Manuscripts are published online shortly after acceptance, before technical editing, formatting and proof reading. Using this free service, authors can make their results available to the community, in citable form, before we publish the edited article. We will replace this *Accepted Manuscript* with the edited and formatted *Advance Article* as soon as it is available.

You can find more information about *Accepted Manuscripts* in the [Information for Authors](#).

Please note that technical editing may introduce minor changes to the text and/or graphics, which may alter content. The journal's standard [Terms & Conditions](#) and the [Ethical guidelines](#) still apply. In no event shall the Royal Society of Chemistry be held responsible for any errors or omissions in this *Accepted Manuscript* or any consequences arising from the use of any information it contains.



Journal Name

ARTICLE

Co-sensitization Promoted Light Harvesting with a New Mixed-Addenda Polyoxometalate $[\text{Cu}(\text{C}_{12}\text{H}_8\text{N}_2)_2]_2[\text{V}_2\text{W}_4\text{O}_{19}]\cdot 4\text{H}_2\text{O}$ in Dye-Sensitized Solar Cells

Received 00th January 20xx,
Accepted 00th January 20xx

DOI: 10.1039/x0xx00000x

www.rsc.org/

Sha-Sha Xu, Wei-Lin Chen,* Yan-Hua Wang, Yang-Guang Li, Zhu-Jun Liu, Chun-Hui Shan, Zhong-Min Su and En-Bo Wang*

A di-vanadium-substituted Lindqvist-type polyoxometalate $[\text{Cu}(\text{C}_{12}\text{H}_8\text{N}_2)_2]_2[\text{V}_2\text{W}_4\text{O}_{19}]\cdot 4\text{H}_2\text{O}$ (**1**) was hydrothermally synthesized and characterized structurally by single crystal X-ray diffraction analysis. X-ray photoelectron spectroscopy and Energy disperse spectroscopy tests further prove the existence of vanadium. Ultraviolet photoelectron spectroscopy and Density Functional Theoretical studies indicate that the energy level of **1** matches well with the conduction band of the TiO_2 . Furthermore, considering the semiconductor-like nature of **1** and the introduction of transition metal element Cu synchronously extends the absorption to the visible region, which should also be beneficial to the photovoltaic device performance. **1**-doped TiO_2 composites (denoted as **1**@ TiO_2) have been successfully fabricated by a simple sol-gel method, which were introduced into the dye-sensitized solar cells (DSSCs) as co-sensitizers in N719-sensitized photoanodes by mixing **1**@ TiO_2 with P25 nanoparticles with different weight ratios to enhance the photoelectric conversion efficiency. The investigations show that the DSSC assembled with **1**@ TiO_2 /19P25 photoanode has the best performance and the overall improvement of the efficiency is 21.6% compared with pure P25. Furthermore, the electrochemical impedance spectroscopy and open-circuit voltage decay investigations show that the co-sensitization of **1** and N719 can promote electron transfer and restrain charge recombinations in the DSSCs, resulting in the longer electron lifetime.

Introduction

The dye-sensitized solar cells (DSSCs) have attracted extensive attention due to their low cost, long-term stability, easy fabrication process and high power conversion efficiency.¹ Typically, the configuration of DSSCs comprises a dye-sensitized photoanode, a Pt counter electrode and an electrolyte with a redox couple. As one of the key parts in DSSCs, the sensitizer is important for high power-conversion efficiency, since they trigger and maintain the electron transfer processes in a photo electro chemical system by absorbing solar radiation.² Up to now, the efficiency of DSSCs sensitized by N719 has reached up to 11–12%. However, N719 shows a narrow spectral response (300–550 nm),^{3a} which is smaller than crystalline silicon (500–1100 nm).^{3b} Their photon harvesting mainly in visible region is one of the major

stumbling blocks for the further enhancement in the photo conversion efficiency. Thus it is necessary to explore novel panchromatic sensitizer, which can cover as much as the whole visible light and even near-infrared region to improve the overall efficiency. But it is presently a substantial challenge using a single dye. The co-sensitization of multiple dyes paves a new approach to obtaining a broader and more intense absorption band, finally increasing the performance of the DSSCs.⁴ As far as we know, an excellent candidate for co-sensitization should possess the following essential characteristics: (a) the lowest unoccupied molecular orbital (LUMO) energy level should be higher than the conduction band (CB) edge of TiO_2 semiconductor for the efficient electron injection; (b) the highest occupied molecular orbital (HOMO) energy level should be lower than the redox mediator for the efficient electron reduction in dye regeneration; (c) the absorption spectrum of the sensitizer should range for the whole visible and even the near-infrared region; (d) the sensitizer should be photostable, electrochemical and thermal stable. On the basis of the above considerations, it is important to investigate new dyes to improve the efficiency of DSSCs.⁵

Polyoxometalates (denoted as POMs), as a large and rapidly growing class of inorganic metal-oxygen nanoclusters based mainly on W, Mo, and V, have been widely studied including their catalysis, electronic and redox properties.⁶ There are empty *d* orbitals in the structures of polyoxoanions, which can

^aKey Laboratory of Polyoxometalate Science of Ministry of Education, Department of Chemistry, Northeast Normal University, Changchun 130024 (P. R. China). E-mail: chenwl@nenu.edu.cn, wangeb889@nenu.edu.cn, wangeb889@hotmail.com,

Electronic Supplementary Information (ESI) available: the BVS, XPS, EDX, IR, UV-Vis, TGA and XRD characterization; current–voltage characteristics; equivalent circuit; fitted parameters; emission spectrum of phen; selected bond lengths and bond angles. CCDC 1412746. For ESI and crystallographic data in CIF or other electronic format see DOI: 10.1039/x0xx00000x

undergo a stepwise multi-electron reversible redox reaction and retain the original structure.⁷ POM-doped TiO₂ photoanodes have been applied in the DSSCs, since POMs are good electron acceptors, which can promote the electron-transfer rate of the CB of TiO₂ to inhibit the electron reflux to enhance photoelectric conversion efficiency.^{8a} However, the LUMO of most of the POMs is lower than the CB of the TiO₂, so there are few reports on the POM-based sensitizer.^{5,8b} So it is still a challenge to regulate the electronic characteristics and energy levels of POMs. As far as we know, the electronic characteristics and redox properties of POMs would be changed by combined with organic groups to adjust the surface oxygen density of POMs.⁹ In addition, the absorption spectrum of the POMs can be controlled by introducing transition metal elements, which can even cover the visible light spectrum.⁵ Up to date, many heteropolytungstates-based organic-inorganic hybrid compounds have been reported, but the hybrids based on the [W₆O₁₉]²⁻ and V-substituted Lindqvist-type [V_xW_(6-x)O₁₉]ⁿ⁻ as inorganic building blocks are still scarce.¹⁰ The main reason is that some of these isopolyoxoanions are metastable intermediates or low concentration fragments in solution, which cannot be stabilized or isolated from the common reaction systems.¹¹ Generally, the hydrothermal environment may change the equilibrium phases of the POM reaction system from the thermodynamically stable compounds to the kinetically stable species.¹² Although [Cu(phen)₃][W₆O₁₉] was synthesized,^{10b} in which the polyoxotungstate subunit only acted as a discrete cluster and modified by organic ligands on its surface, no inorganic ligand to link the metal centers. That is there were no covalent bonds linked between the organic and the inorganic parts. As far as we know, the substitution of tungsten atoms by low-valent metal atoms (V, Nb, or Ta) may lead to an increase in the surface electric charge density of polyoxoanions, which makes the coordination fashions more flexible.¹³

Here, we synthesized a new mixed-addenda polyoxometalate [Cu(C₁₂H₈N₂)₂]₂[V₂W₄O₁₉]·4H₂O (**1**) using hydrothermal method, which was characterized structurally by the single crystal X-ray diffraction. Ultraviolet Photoelectron Spectroscopy (UPS) and Density Functional Theory (DFT) were conducted to determine the energy levels. Furthermore, the **1**-doped TiO₂ (denoted as **1**@TiO₂) and commercial P25 composites with different weight ratios were introduced to the photoanodes of DSSCs to explore efficiency of the **1** and N719 cosensitized cells, owing to the semiconductor-like nature of **1**, its higher LUMO level and smaller band gap than TiO₂. The cosensitization of **1** and N719 enhanced the photoelectric conversion efficiency of the DSSCs.

Results and discussion

Crystal structure

Compound **1** was successfully prepared under hydrothermal condition at 160°C at a limited pH range of 8.1-8.5. Single crystal X-ray diffraction analysis reveals that compound **1**

crystallizes in the monoclinic space group C2/c, which is composed of a di-V substituted classical Lindqvist-type polyanion [V₂W₄O₁₉]⁴⁻ and two [Cu(phen)₂]²⁺ units (Fig. 1a). The W₁/V₁ and W₂/V₂ positions were simultaneously statistically occupied by V^V and W^{VI} elements with half occupancy for each, resulting in two V^V ions per Lindqvist cage. The oxidation state of W, V and Cu are determined on the basis of the crystal color, bond lengths, X-ray photoelectron spectroscopy (XPS), charge balance consideration as well as bond valence sum calculations (BVS) (a detailed survey in Supporting Information, Table S1†). All the results indicated that the W, V and Cu sites possess +6, +5 and +2 oxidation states, respectively. The Cu atom is five-coordinate in elongated octahedral coordination environment: four nitrogen atoms from two bidentate chelating phenanthroline ligands and one bridge oxygen from [V₂W₄O₁₉]⁴⁻ anion form a {CuN₄O} square pyramid. Such an unusual linking fashion is unique in the polyoxometalate chemistry. The bond lengths comparisons of M-O (M=W, V) in **1** with those of [W₆O₁₉]²⁻ and some reported [V₂W₄O₁₉]⁴⁻ structures are listed in Table S2†, which shows that the bond distance of M-O in **1** is comparable to those of previously reported [V₂W₄O₁₉]⁴⁻. In the packing arrangement of **1**, the adjacent POMs anions are connected with phenanthroline molecules by the aromatic π-π stack interactions to form an open-framework viewed along [0, 2, 1] and c axis direction (Fig. 1b, Fig. S1†).

XPS and EDX

The XPS spectra of the C, Cu, V and W are depicted in Fig. S2†.

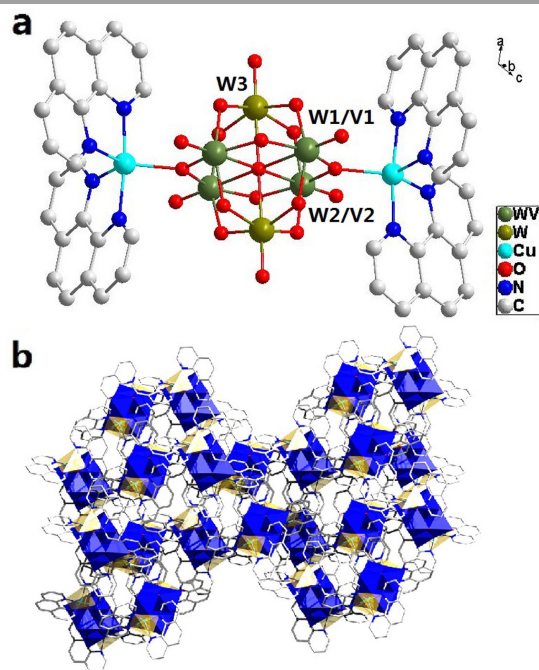


Fig. 1 (a) ball and stick representation of **1**. (b) Packing arrangement of **1** viewed along [0, 2, 1] direction. Color codes: {CuON₄}, yellow polyhedron; {W(V)O₆}, blue octahedron; C (grey); N (blue).

XPS analyses were corrected with reference to C1s (284.6 eV). The 934.32 and 954.49 eV binding energies correspond to the spin orbit splitting components of Cu2p_{3/2} and Cu2p_{1/2} in +2 oxidation state.^{14a} The binding energies of 33.8 and 35.9 eV are attributed to W4f_{7/2} and W4f_{5/2} of the polyoxoanions, which is consistent with the W^{VI} oxidation state.^{14a} The XPS spectrum for V2p shows two peaks at ca. 517 and 524 eV in the energy regions of V2p_{3/2} and V2p_{5/2}, separately, which correspond to the V^V oxidation state.^{14b} These results are consistent with BVS calculations from the X-ray structural analysis data. The composition of **1** was also examined by the energy dispersive X-ray (EDX) analysis to prove the existence of vanadium (Fig. S3†). It demonstrates the existence of C, N, O, Cu, V and W, and confirms the presence of two vanadium atoms as well as four tungsten atoms in the common cluster anion of **1**.

IR spectra and UV-Vis spectroscopy

The IR spectra of **1**, TiO₂ and **1**@TiO₂ are shown in Fig. S4†. In the IR spectrum of **1**, the vibrations in the region of 1521–1103 cm⁻¹ can be attributed to the characteristic peaks of phenanthroline (denoted as phen). The presence of the [V₂W₄O₁₉]⁴⁻ anion in **1** is illustrated by the strong IR absorption bands at 954 cm⁻¹, 762 cm⁻¹ and 579 cm⁻¹ regions, which are ascribed to the M–O_t and M–O_b (M=W or V) vibrations, respectively,^{10a} which are in good agreement with the compound K₄V₂W₄O₁₉·8H₂O.¹⁵ As for the IR of **1**@TiO₂/19P25, it can be observed that several characteristic peaks of **1** in the photoanode although the pure P25 peaks are too strong, which indicate that **1** maintains its structure integrity in the photoanode.

The diffuse reflectance UV-Vis spectrum of **1** was tested with a solid state sample (Fig. S5†). The higher energy bands (225 nm and 414 nm) are mainly attributed to the O→W/V charge transfer transition of [V₂W₄O₁₉]⁴⁻ units, whereas the lower energy band (756 nm) is ascribed to the metal *d-d* charge transfer.¹⁶ Moreover, the lower energy band of 756 nm shows significantly enhanced absorption in the visible region beyond 400 nm, which may benefit the photoelectrocatalytic activity.

Thermogravimetric analysis and XRD analyses

Thermogravimetric analysis (TGA) of **1** was carried out to study its thermal stability (Fig. S6†). The TGA curve of **1** exhibits two continuous steps of weight loss. An initial weight loss of 5.9% below 98.3°C is from the release of the lattice water (calcd. 3.5%). On further heating, the second weight loss occurs between 365 °C to 600 °C, corresponding to the loss of the phen ligands on the copper centers. The first step of data error may be that it adsorbed water molecules based on the elemental analyses and crystallographic analyses.

X-ray diffraction analysis (XRD) was performed to check the homogeneity of the crystalline and the bulk phase of **1**. The peaks positions of the experiment are in good agreement with the simulated one based on the data of single-crystal structure, indicating the purity of the as-synthesized products (Fig. S7†). The differences in reflection intensity are probably due to

preferential orientations in the powder sample of **1**. Besides, we tested the XRD pattern of the **1**@TiO₂/19P25 composite to prove the anatase phase of TiO₂ composite. The characteristic peaks 25.3°, 37.9°, 48.0°, 54.1°, 54.9°, 62.7°, 68.6°, 70.3° and 74.7° are observed from Fig. S8†, which are in agreement with those of anatase TiO₂ reported in literatures, which is the favorite phase for the photoanode of DSSCs.¹⁷

Frontier molecular orbital energies of **1**

In order to provide the thermodynamic driving force for charge generation, the molecular orbital of **1** was preliminarily studied by means of DFT calculations (Fig. 2), which illustrates that optical irradiation would induce electronic transmission from the [Cu(phen)₂]²⁺ unit to [V₂W₄O₁₉]⁴⁻. The LUMO level of **1** is -2.992 eV, which is higher than the CB of TiO₂ (-4.0 eV). It suggests that **1** should be capable of injecting electrons into the CB of TiO₂. The HOMO level of **1** (-5.437 eV) remains below the redox level (-4.60 eV) for efficient regeneration of the dyes.¹⁸ The HOMO-LUMO energy gap (*E_g*) of **1** is about 2.445 eV, demonstrating it exhibits the semiconductor-like feature. It is known that a narrower band gap normally results in stronger visible response. So these characteristics render compound **1** the fundamental feasibility to be a potential useful sensitizer for the photovoltaic application.

Optical energy gap and UPS

The optical band gap was obtained through the diffuse reflectance UV-Vis spectrum for a powder sample to explore the conductivity of **1**. First, a plot of Kubelka–Munk function *F* against energy *E* was drawn, in which $F = (1-R)^2/2R$ and *R* is the reflectance of an infinitely thick layer at a given wavelength. The band gap (*E_g*) is determined as the intersection point between the energy axis and the line extrapolated from the linear portion of the absorption edge in the plot of Kubelka–Munk function *F* against energy *E*.¹⁹ Several POM-based inorganic–organic hybrid compounds have been reported to

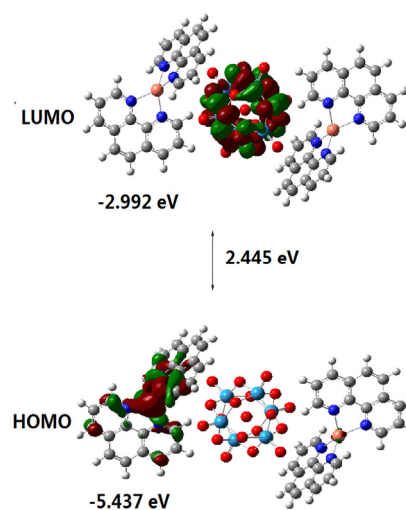


Fig. 2 Frontier molecular orbitals of **1**

be promising semiconductors, such as $\text{Co}_2(\text{bpy})_6(\text{W}_6\text{O}_{19})_2$ ($E_g = 2.2$ eV).²⁰ As can be seen in Fig. 3a, E_g is assessed at 2.49 eV, which is smaller than TiO_2 (3.2 eV).

The UPS spectrum is shown in Fig. 3b. The work function (W_F) of **1** surface can be directly obtained by measuring the secondary electron cut off of the photoemission spectrum, which gives a W_F value around 4.08 eV. By adding the binding energy of the onset of the band of occupied orbitals, the ionization energy (I_E) of **1** was estimated, which gives the position of the HOMO with respect to the vacuum level.²¹ On the basis of the UPS results and the E_g (2.49 eV) estimated by Tauc plot analysis of absorption measurement, the LUMO level of **1** (-3.265 eV) can be calculated. It is concluded that the LUMO level of **1** lies overtop the TiO_2 . All the results give good qualitative agreement with theoretical calculation. The slight difference of the theoretical calculations and experimental data can be attributed to the neglect of solvent effect in theory calculation.

Photovoltaic performance investigations of DSSC

SEM images of the composite films can examine the intrinsic morphology and the dispersion of particles in the photoanodes. The pure TiO_2 film was observed to have an average diameter of ca. 30–45 nm (Fig. 4A and 4B). Some big blocks among TiO_2 particles in the **1**@ TiO_2 composite can be observed compared to the bare P25 (Fig. 4C and 4D). Most of the particles disperse evenly in the photoanodes, and the particle sizes become larger after doping with POMs, which also confirms that **1** was doped in the photoanodes.

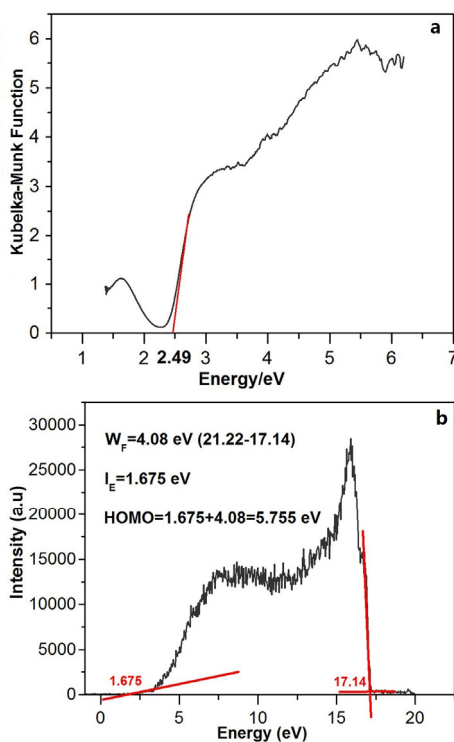


Fig. 3 Energy gap (a) and UPS photoemission spectrum (b) of **1**

Compound **1** and N719 cosensitized photoanodes were assembled into the sandwich DSSCs, their performances were investigated under the simulated AM 1.5 illuminations (100 mW cm^{-2}). All the datas of DSSCs were the average of three experimental values and the absolute deviation were calculated. The influence of the amount of **1** for the overall improvement of the efficiency of DSSCs was investigated (Fig. S9†). The DSSCs performance parameters are listed in Table 1. It can be observed that the performance of the DSSCs with **1**@ TiO_2 /19P25 is much higher than other weight ratios. A short-circuit current density (J_{sc}) of 16.71 mA/cm^2 and an open-circuit voltage (V_{oc}) of 0.691 V were produced with a fill factor (FF) of 0.609, for a power conversion efficiency (η) of 7.05%, which is better than the pure P25. The main reason results may be speculated that the **1**-doped TiO_2 could absorb more visible light due to its smaller band gap of **1** than TiO_2 , which endowed the cosensitized solar cell with more sunlight absorption. The photocurrent–voltage (J – V) results in Fig. 5a show that the performance of the DSSCs with **1** and N719 cosensitization (**1**@ TiO_2 /19P25) was enhanced compared to the single N719 (pure P25). As far as **1**@ TiO_2 /3P25 performance is lower than the pure P25, which may be ascribed to the aggregation of the particles induced by the larger amount of **1**@ TiO_2 composite.^{8a} The inset figure of Fig. 5a shows the current–voltage characteristics in the dark, which implies that the dark current of **1**@ TiO_2 /nP25 cells have been largely reduced compared to the pure P25, which may be attributed to the fact that the blocking of POMs prevent the electron from flowing back to electrolyte or dyes with the oxidation state.

Electrochemical impedance spectroscopy (EIS) of the DSSCs is widely used to study the electron transport property and the internal resistances of the DSSCs.²² The EIS of the DSSCs with N719 sensitized cell (pure P25) and **1**/N719 cosensitized cell (**1**@ TiO_2 /19P25) were conducted (Fig. 5b). Table S3† lists the parameters obtained by fitting the impedance spectra of the composite solar cells using the equivalent circuit (see the Fig. S10†). The series resistance (R_s) can account for the resistance of the FTO glass substrate, the contact resistance of the cell and the resistance of the external circuits. There are two sets of semicircles from high to low frequency, which are classically assigned to the charge-transfer resistance at the counter photoanode/electrolyte interface (R_2) and the recombination kinetics at the TiO_2 -electrolyte interface (R_1).^{8a}

Table 1 Photovoltaic properties of the DSSCs based on different photoanodes. The value of the data in the table was obtained from the average of three parallel DSSCs.

	J_{sc} (mA cm^{-2})	V_{oc} (V)	FF (%)	η (%)
pure P25	13.02±0.01	0.673±0.003	0.603±0.001	5.80±0.02
1 @ TiO_2 /19P25	16.71±0.02	0.691±0.003	0.609±0.002	7.05±0.01
1 @ TiO_2 /7P25	15.95±0.02	0.693±0.004	0.601±0.001	6.62±0.01
1 @ TiO_2 /5P25	15.25±0.01	0.662±0.002	0.561±0.002	5.64±0.02

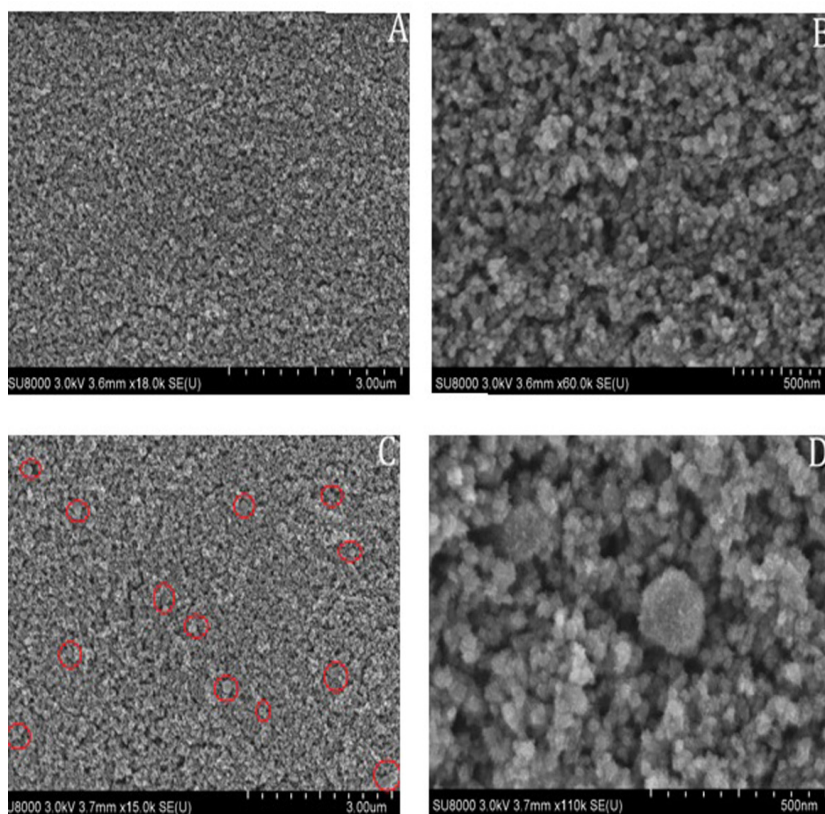


Fig. 4 (A) and (B) SEM images of N719 sensitized cell; (C) and (D) of **1**/N719 cosensitized cell.

As shown in Fig. 5b, the R_2 is similar since all the cells have the same Pt counter and electrolyte. However, the **1**/N719 cosensitized cell has larger R_1 than that of the N719 sensitized cell. The increasing of resistance at the TiO_2 -electrolyte interface is in favour of suppressing charge recombination for improving the J_{sc} . Besides, the Bode phase plot also shows the results of the EIS (Fig. 5c). The mean electron lifetime (τ_e) can be calculated from the formula: $\tau_e = \omega \text{min}^{-1} = (2\pi f_{\text{max}})^{-1}$, f_{max} is the frequency at the top of the intermediate frequency arc.²³ The electron lifetime of the **1**/N719 cosensitized cell was longer than that of N719 sensitized cell (see Table S3†), which indicates that **1**@ TiO_2 to the photoanode may inhibit the recombination of the electrons with the oxide electrolyte, resulting in a longer electron lifetime. The carriers recombining with the electrolyte can be further revealed by the open-circuit voltage decay (OCVD) when turning off the illumination in a steady state and detecting the decay of photovoltage.²⁴ The photocurrent response curve of **1**/N719 cosensitized cell displays significantly higher photocurrent than that of N719 sensitized cell, indicating that the excited electrons in **1** transfer to TiO_2 upon excitation. The electron lifetime is

obtained according to the following formula: $\tau_e = (kT/e) \times (dV/dt)^{-1}$.²⁵ As can be seen in the Fig. 5d, **1**/N719 cosensitized cell decays more slowly than N719 sensitized cell, which indicates that their charge recombination rate is much slower. This variation trend is in accordance with the results of the EIS and the dark current analyses. Fig. 6 shows the mechanism of electrons transfer pathways in the **1**/N719 cosensitized cell. In DSSCs, the LUMO level of **1** is higher than the CB of TiO_2 , the **1** and N719 dyes are excited by absorbing photon and then they form oxidized dyes after injection of the electron into the CB of photoanode. The HOMO level of **1** and N719 dyes are positive with respect to the energy level of iodine/iodide redox couple in quasi-solid state electrolyte, so the oxidized dyes accepted electron from the I_3^-/I^- to be regenerated. Higher efficiency values of DSSCs might be due to both the smaller band gap of **1** than TiO_2 and better UV/Visible absorption, finally accelerating electron transmission in the photoanode. Moreover, the introduction of POMs may inhibit the electron recombinations with the oxide electrolyte, resulting in a longer electron lifetime.

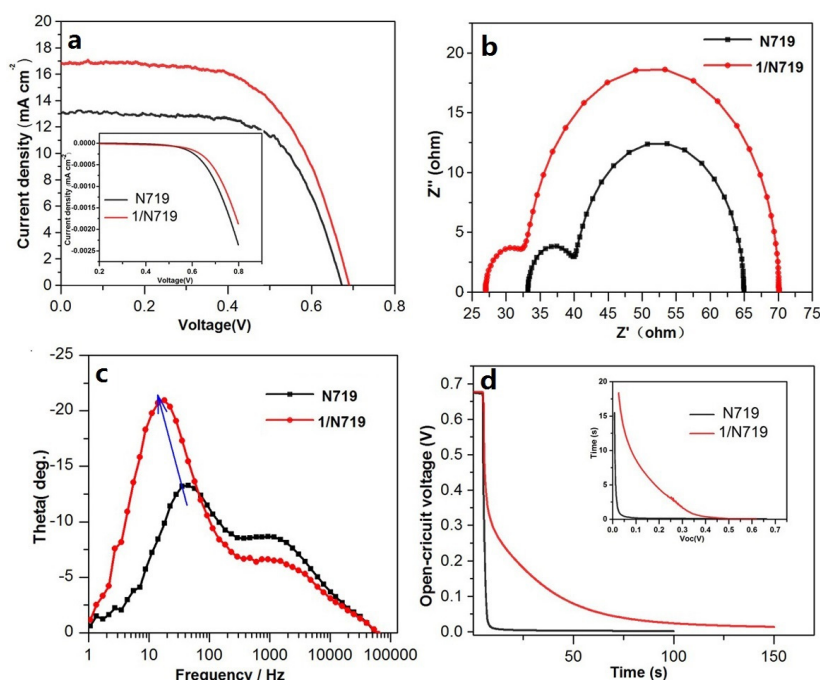


Fig. 5 (a) Current–voltage curves under AM 1.5 illumination and in the dark (inset) of DSSCs with N719 (dark line) and 1/N719 (red line) sensitization. (b) The EIS spectra of N719 (dark line) and 1/N719 (red line)-based DSSCs. (c) Bode phase plots. (d) OCVD spectra of DSSCs based on N719 (dark) and 1/N719 (red). The inset is their corresponding electron lifetime.

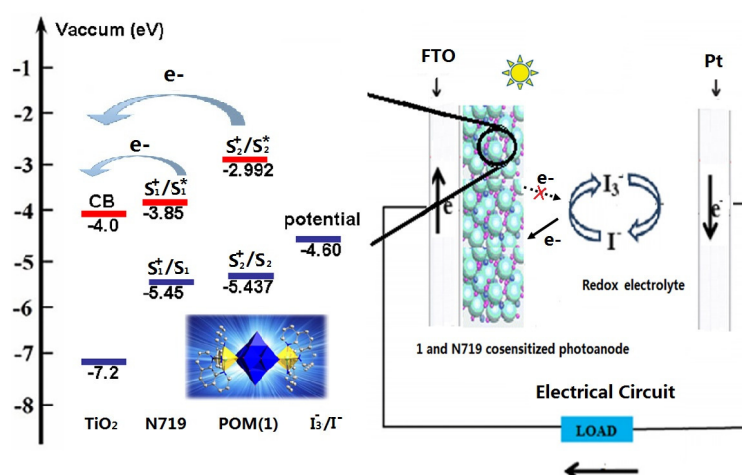


Fig. 6 Mechanism of photoinduced electron flow through the 1 and N719 cosensitized cell.

Fluorescence properties

The excitation and emission spectra of compound **1** were investigated to explore its potential applications as the luminescent crystalline materials, which were tested in the solid state and in the DMSO solution at room temperature, respectively. The emission and excitation spectra of **1** in the

solid state (Fig. 7a) exhibit an emission maximum at 338 nm upon the excitation at 291 nm. Besides, the emission and excitation spectra of **1** tested in the DMSO show two main emission peaks at 410 nm and 438 nm, and a shoulder peak at 459 nm upon the excitation wavelength at 290 nm (Fig. 7b). A red shift of the peak can be observed in DMSO solution

emission spectra compared to the emission spectra measured in the solid state, the reason of which may be that the fluorescence wavelength has a red shift with the increasing of polarity of the solvents.²⁶

In order to study the active luminescent group in **1**, the luminescent properties of phen and $K_4[V_2W_4O_{19}]\cdot 8H_2O$ were also tested under the identical experimental conditions. The free phen ligand was investigated upon the excitation at 320 nm (Fig. S11[†]), four obvious emissions at 363 nm, 381 nm, 404 nm, 430 nm are observed. It is worthy to mention that the emission band of the phen ligand can be attributed to a $\pi-\pi^*$ or $n-\pi^*$ electronic transition within the aromatic systems. However, $K_4[V_2W_4O_{19}]\cdot 8H_2O$ shows no luminescent property. On the basis of these experimental results, it can be presumed that the luminescent properties of **1** are mainly attributed to the ligand-to-metal charge transfer.

It is known that the fluorescence lifetime can often establish time scales for photo electrochemistry or electron transfer.²⁷ The time-resolved fluorescence decay was recorded at room temperature with emission monitored at 440 nm ($\lambda_{Ex} = 290$ nm) with a pulsed light source. The luminescence decay profile is given in Fig. 8. The line is the best fit to the data using a double-exponential decay function: $I(t) = A + B_1 \exp(-t/\tau_1) + B_2 \exp(-t/\tau_2)$, Where B_1 and B_2 are the relative amplitudes, τ_1 and τ_2 are the component lifetimes, respectively. Average fluorescence lifetime τ is calculated according to the following equation: $\tau = [B_1/(B_1+B_2)] \times \tau_1 + [B_2/(B_1+B_2)] \times \tau_2$.²⁸ According to the experimental results: $\tau_1 = 4.8212$ ns, $\tau_2 = 31.7080$ ns, one accounts for 33.33% of the proportion, another is 69.67%, $B_1 = 536.411$, $B_2 = 187.37$. After calculation, $\tau = 11.7815$ ns ($R^2 = 1.011$).

Experimental

Materials and physical measurement

All chemicals were commercially purchased and used without further purification. $K_4V_2W_4O_{19}\cdot 8H_2O$ was synthesized according to the literature method.¹⁵ The elemental analyses for C, H and N were performed on a Perkin-Elmer 2400 CHN Elemental Analyzer. The elemental analyses for W, V and Cu were performed with a Leaman inductively coupled plasma (ICP) spectrometer. IR spectra were recorded in the range of 400-4000 cm^{-1} on an Alpha Centauri FT/IR Spectrophotometer using KBr pellets. UV-Vis absorption spectra were recorded performed with a Leaman inductively coupled plasma spectrometer. IR spectra were recorded in the range of 400-4000 cm^{-1} on an Alpha Centauri FT/IR Spectrophotometer using KBr pellets. UV-Vis absorption spectra were recorded on a 756 CRT UV-Vis spectrophotometer. The thermogravimetric analysis (TGA) was performed on a Perkin-Elmer TGA7 instrument in flowing N_2 with a heating rate of 10 $^\circ C \cdot min^{-1}$. Powder X-ray diffraction (XRD) pattern was recorded with a D/max-IIIc diffractometer. Photovoltaic tests of the DSSCs were recorded on a CHI601D Electrochemical Workstation. EIS measurements were performed on CS350 electrochemistry station with a Xe lamp and an AM 1.5 solar filter. Scanning

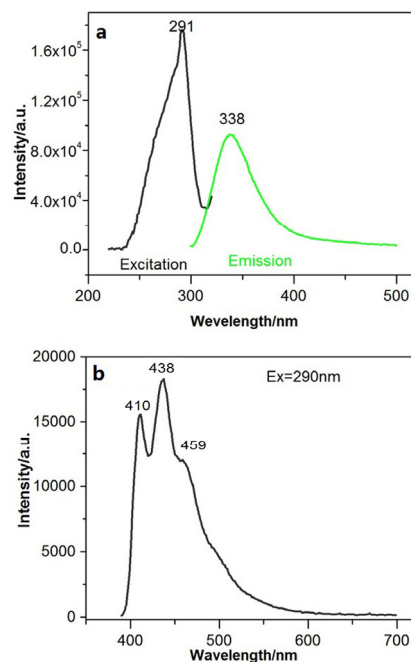


Fig. 7 (a) The excitation spectrum (black, $E_x = 291$ nm) and emission spectrum (green, $E_m = 338$ nm) of **1** in solid state at room temperature; (b) The emission spectrum ($E_x = 290$ nm) of **1** in the DMSO.

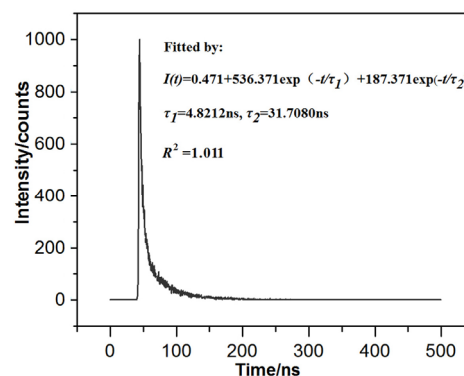


Fig. 8 Decay curve of **1** recorded at room temperature. The line is the best fit to the data using a double-exponential function.

electron microscopy (SEM) images were obtained from FEI Quanta 200F microscope operated at an accelerating voltage of 20kV. Fluorescence spectra were carried out with FLSP920 Fluorescence Spectrometer. The analysis was performed with X-ray photoelectron spectroscopy (XPS) measurements with a hemispherical analyser Leybold EA 11. UPS measurements were performed using a He discharge lamp ($h\nu = 21.22$ eV). For the determination of the position of the high BE cut-off of the UPS spectrum (which reflects the work function of a sample) a bias voltage of 5 V was applied to the sample. The energy and shape of the frontier molecular orbitals of **1** were optimized computed by using the hybrid B3LYP functional and the basis set of SDD containing relativistic effects for W, Cu and 6-31G for C, H and other atoms were applied.

Preparation of 1

A mixture of $\text{Na}_2\text{WO}_4 \cdot 2\text{H}_2\text{O}$ (6.0 g, 18.2 mmol), $\text{CuCl}_2 \cdot 2\text{H}_2\text{O}$ (0.17 g, 1.00 mmol), phen (0.20 g, 1.00 mmol), NH_4VO_3 (0.16 g, 1.37 mmol) and water (200 mL) were stirred at room temperature for 0.5 h. The pH of the solution is 8.1-8.5. Then the above mixture solutions with different acidities were transferred into the Teflon-lined autoclaves and heated at 160°C for 120 h. After the reaction temperature was slowly decreased at a speed of 5°C·h⁻¹ to room temperature. Then the green tubular crystals were isolated and washed with distilled water. The crystals were dried in a desiccator at room temperature with the total yield of 52% based on W. Elemental analysis for $\text{C}_{48}\text{H}_{40}\text{Cu}_2\text{N}_8\text{O}_{23}\text{V}_2\text{W}_4$, Anal. calcd. C 27.94, H 1.97, N 5.43, Cu 6.16, W 35.67, V 4.94(%); Found: C 27.10, H 2.19, N 5.25, Cu 6.02, W 34.71, V 4.79(%)

X-ray crystallography

The suitable single crystal of **1** was glued on a glass fiber. **1** with dimensions of 0.24 mm×0.23 mm×0.22 mm was mounted on a Rigaku RAXIS RAPID IP diffractometer with Mo K α ($\lambda = 0.71073$ Å) at 293 K. An empirical absorption correction was applied. Neither crystal showed evidence of crystal decay during data collections. The structure was solved by the direct method and refined by the full-matrix least-squares method using the SHELXTL crystallographic software package.²⁹ In the refinement, the restraint command ISOR was employed to restrain some non-hydrogen atoms so as to avoid ADP and NDP problems in the crystal data. The hydrogen atoms on the lattice water molecules and the phen ligands were directly included in the final molecular formula. A summary of the crystallographic data and structure refinement is given in Table 2. Selected bond lengths and bond angles of **1** can be seen at Table S4[†]. Further details of the crystal structure can be obtained from The Cambridge Crystallographic Data Center via www.ccdc.cam.ac.uk/data_request/cif with CCDC 1412746.

The preparation of the photoanodes

The synthesis of 1-doped TiO₂ with sol-gel method: In a beaker, 5 mL titaniumtetraisopropoxide (TTIP) was dropped into 3 mL of *n*-butyl alcohol while stirring. In another beaker, 0.05 g **1** was dispersed in the 6 mL water. **1** was treated under ultrasonic irradiation for half an hour in order to completely scattered, and then added it into the TTIP solution drop by drop.^{30a} After the ivory turbid liquid was heated at 45°C for 3 h and at 80°C for about 3 h until a hydrogel formed. The hydrogel was transferred into a 45°C vacuum oven and heated for 12 h and then at 80°C for 3 h. The product is green powder.

The fabrication of DSSCs

The photoanode film was assembled using a screen printing technology. Before the screen printing process, the F-doped SnO₂-coated conductive glass plates (FTO) were immersed in 40 mmol TiCl₄ aqueous solution at 70°C for 30 min and washed with water and ethanol to form a compact layer. In the preparation of the photoanode, due to the phen of **1** was decomposed in the 360°C, in order to keep the integrality of

Table 2 Crystal data and structure refinements for **1**

Compound 1	
Chemical formula	$\text{C}_{48}\text{H}_{40}\text{Cu}_2\text{N}_8\text{O}_{23}\text{V}_2\text{W}_4$
Formula weight (<i>M</i>)	2061.24
Temperature (<i>K</i>)	296(2)
Crystal system	Monoclinic
Space group	C2/c
<i>a</i> (Å)	27.888(3)
<i>b</i> (Å)	15.5043(16)
<i>c</i> (Å)	14.6345(15)
α /(°)	90
β /(°)	117.0380(10)
γ /(°)	90
<i>V</i> (Å ³)	5700.3(7)
<i>Z</i>	4
<i>D_c</i> (g/cm ³)	2.429
<i>R</i> ₁	0.0564
<i>wR</i> ₂	0.1482
$R_1 = \sum F_o - F_c / \sum F_o $. $wR_2 = \sum [w(F_o^2 - F_c^2)^2] / \sum [w(F_o^2)^2]^{1/2}$	

the **1**, so we firstly sintered the TiO₂ at 450°C in a muffle furnace to ensure that the TiO₂ composite is anatase. The **1**-doped TiO₂ (denoted as **1**@TiO₂) and commercial P25 composites with different weight ratios were introduced to the photoanodes of DSSCs. Then we prepared the paste based on the literatures,^{30b} a layer of paste was coated on the FTO glass plates by screen-printing, and then dried for 5 min at 120°C to make the ethanol volatilization. The screen printing procedure was repeated four times. An 8-12 μm thickness with an area of 0.1 cm² was printed onto FTO and sintered at 320°C for 30 min by the temperature programmed (at 275°C for 5 min, at 300°C for 5 min, at 320°C for 30 min). Following, the FTO glass plates were again immersed into 40 mmol TiCl₄ aqueous solution at 70°C for 30 min. Finally the FTO glass plates were calcined once again following the same steps. Thereafter, the calcined photoanode was immersed in absolute ethanol solution containing 0.3 mM N719 for 24 h to adsorb enough dyes as the co-sensitizer. The non-adsorbed dyes were removed with absolute ethanol and dried under nitrogen flow at room temperature. **1**/N719 cosensitized photoanode and Pt counter electrode were assembled in sandwich shape. An electrolyte containing 0.5M LiI, 0.05M I₂, and 0.1M TBP (4-tert-butylpyridine) were added to the cell.

Conclusions

In summary, a di-vanadium-substituted Lindqvist-type organic-inorganic hybrid compound $[\text{Cu}(\text{C}_{12}\text{H}_8\text{N}_2)_2]_2[\text{V}_2\text{W}_4\text{O}_{19}] \cdot 4\text{H}_2\text{O}$ was designed and synthesized. Its semiconductor-like property was investigated by UPS and DFT calculations, which indicate that it possesses a smaller band gap and higher LUMO than that of TiO₂. In addition, the introduction of transition metal

Cu extends the absorption to the visible region, which should also be beneficial for the photovoltaic device performance. 1/N719 cosensitized solar cell configuration was constructed to detect the synergistic effect of 1/N719, which significantly improved the solar-to-electrical energy conversion efficiency compared with the N719 sensitization. This enhancement of the energy conversion efficiency may be due to the smaller band gap of **1** than TiO₂ and better UV/Visible absorption, finally accelerating electron transmission in the photoanode. These results indicate that the refinements in the structure, composition and carrier separation of POMs would provide a basis for exploring POM-based co-sensitizers to improve the solar energy conversion efficiency. Besides, compound **1** also exhibits fluorescent properties, which may be used as potential photo-active materials. Further efforts will be focused on the construction of transition metal complexes by selecting other organic ligands and POMs building blocks, leading to functional POMs-based metal-organic hybrid complexes.

Acknowledgements

This work was financially supported by the National Natural Science Foundation of China (No. 21131001 and 21201031), the Open Subject Foundation of Key Laboratory of Polyoxometalate Science of Ministry of Education, the Science and Technology Research Foundation of the Thirteenth Five Years of Jilin Educational Committee, the Technology Foundation for Selected Overseas Chinese Scholars, Ministry of Personnel of China and the Analysis and Testing Foundation of Northeast Normal University.

Notes and references

- (a) B. O'regan and M. Grätzel, *Nature*, 1991, **353**, 737; (b) Q. Yu, Y. Wang, Z. Yi, N. Zu, J. Zhang, M. Zhang and P. Wang, *ACS Nano*, 2010, **4**, 6032; (c) Y. Qiu, W. Chen and S. Yang, *Angew. Chem., Int. Ed.*, 2010, **49**, 3675; (d) A. Yella, H. W. Lee, H. N. Tsao, C. Yi, A. K. Chandiran, M. K. Nazeeruddin, E. W. Diau, C. Y. Yeh, S. M. Zakeeruddin and M. Grätzel, *Science*, 2011, **334**, 629.
- (a) N. Robertson, *Angew. Chem. Int. Ed.*, 2006, **45**, 2338; (b) J. Luo, M. Xu, R. Li, K. W. Huang, C. Jiang, Q. Qi, W. Zeng, J. Zhang, C. Chi, P. Wang and J. Wu, *J. Am. Chem. Soc.*, 2014, **136**, 265.
- (a) Y. X. Jiang, Y. L. Yang, L. S. Qiang, R. Q. Fan, H. P. Ning, L. Li, T. L. Ye, B. Yang and W. W. Cao, *J. Power Sources.*, 2015, **278**, 527; (b) G. Smestad, C. Bignozzi and R. Argazzi, *Sol. Energy Mater. Sol. Cells.*, 1994, **32**, 259.
- (a) J. H. Yum, S. R. Jang and M. Grätzel, *Chem. Commun.*, 2007, 4680; (b) H. N. Miras, L. Vila-Nadal and L. Cronin, *Chem. Soc. Rev.*, 2014, **43**, 5679.
- J. S. Li, X. J. Sang, W. L. Chen, L. C. Zhang, Z. M. Su, C. Qin and E. B. Wang, *Inorg. Chem. Commun.*, 2013, **38**, 78.
- (a) D. L. Long, R. Tsunashima and L. Cronin, *Angew. Chem. Int. Ed.*, 2010, **49**, 1736; (b) H. N. Miras, L. Vilà-Nadala and L. Cronin, *Chem. Soc. Rev.*, 2014, **43**, 5679; (c) X. L. Wang, T. J. Li, A. X. Tian, N. Li, Y. Yang, Y. L. Ning and X. Hou, *CrystEngComm.*, 2015, **17**, 3257; (d) J. Zhang, F. P. Xiao, J. Hao and Y. G. Wei, *Dalton Trans.*, 2012, **41**, 3599; (e) P. C. Yin, P. F. Wu, Z. C. Xiao, D. Li, E. Bitterlich, J. Zhang, P. Cheng, D. V. Vezenov, T. B. Liu and Y. G. Wei, *Angew. Chem., Int. Ed.*, 2011, **123**, 2569; (f) H. Liu, C. H. Hsu, Z. W. Lin, W. P. Shan, J. Wang, J. Jiang, M. J. Huang, B. Lotz, X. F. Yu, W. B. Zhang, K. Yue and S. Z. D. Cheng, *J. Am. Chem. Soc.*, 2014, **136**, 10691.
- H. Park and W. Choi, *J. Phys. Chem. B*, 2003, **107**, 3885.
- (a) S. M. Wang, L. Liu, W. L. Chen, E. B. Wang and Z. M. Su, *Dalton Trans.*, 2013, **42**, 2691; (b) X. J. Sang, J. S. Li, L. C. Zhang, Z. J. Wang, W. L. Chen, Z. M. Zhu, Z. M. Su and E. B. Wang, *ACS Appl. Mater. Interfaces*, 2014, **6**, 7876.
- C. Boglio and K. Micoine, *J. Am. Chem. Soc.*, 2008, **130**, 4553.
- (a) P. T. Ma, C. F. Yu, J. W. Zhao, Y. Q. Feng, J. P. Wang and J. Y. Niu, *J. Coord. Chem.*, 2009, **62**, 3117; (b) F. X. Meng, K. Liu, Y. G. Chen, *Chinese J. Struct. Chem.*, 2006, **25**, 837; (c) C. Wang, *Asian J Chem*, 2009, **21**, 4755.
- G. Yan, X. Wang, Y. Y. Ma, X. Cheng, Y. H. Wang and Y. G. Li, *Solid. State. Sci.*, 2013, **17**, 146.
- A. X. Tian, Y. L. Ning, J. Ying, J. W. Zhang, X. Hou, T. J. Li and X. L. Wang, *Dalton Trans.*, 2015, **44**, 10499.
- C. L. Wang, L. H. Weng, Y. H. Ren, C. B. Du, B. Yue, M. Gu and H. Y. He, *Z. Anorg. Allg. Chem.*, 2011, **637**, 472.
- (a) J. W. Zhao, Y. Z. Li, F. Ji, J. Yuan, L. J. Chen and G. Y. Yang, *Dalton Trans.*, 2014, **43**, 5694; (b) L. Chen, F. L. Jiang, Z. Z. Lin, Y. F. Zhou, C. Y. Yue and M. C. Hong, *J. Am. Chem. Soc.*, 2005, **127**, 8588.
- C. M. Flynn and M. T. Pope, *Inorg. Chem.*, 1971, **10**, 2524.
- W. L. Chen, Y. H. Wang, Y. G. Li, E. B. Wang and Y. W. Li, *J. Coord. Chem.*, 2009, **62**, 1035.
- L. Li, Y. L. Yang, R. Q. Fan, X. Wang, Q. M. Zhang, L. Y. Zhang, B. Yang, W. W. Cao, W. Z. Zhang, Y. Z. Wang and L. Q. Ma, *Dalton Trans.*, 2014, **43**, 1577.
- B. Basheer, D. Mathew, B. K. George and C. P. R. Nair, *Sol Energy.*, 2014, **108**, 479.
- A. Hiskia, A. Mylonas and E. Papaconstantinou, *Chem. Soc. Rev.*, 2001, **30**, 62.
- L. J. Zhang, Y. G. Wei, C. C. Wang, H. Y. Guo and P. Wang, *J. Solid. State. Chem.*, 2004, **177**, 3433.
- M. Vasilopoulou, A. M. Douvas, L. C. Palilis, S. Kennou and P. Argitis, *J. Am. Chem. Soc.*, 2015, **137**, 6844.
- M. Adachi, M. Sakamoto, J. Jiu, Y. Ogata and S. Isoda, *J. Phys. Chem. B*, 2006, **110**, 13872.
- Q. Wang, J. E. Moser and M. Grätzel, *J. Phys. Chem. B*, 2005, **109**, 14945.
- A. Zaban, M. Greenshtein and J. Bisquert, *ChemPhysChem*, 2003, **4**, 861.
- J. Bisquert, A. Zaban, M. Greenshtein and I. Mora-Sero, *J. Am. Chem. Soc.*, 2004, **126**, 13550.
- Q. Tang, S. X. Liu, D. D. Liang, F. J. Ma, G. J. Ren, F. Wei, Y. Yang and C. C. Li, *J. Solid. State. Chem.*, 2012, **190**, 85.
- M. D. Allendorf, C. A. Bauer, R. K. Bhakta and R. J. T. Houk, *Chem. Soc. Rev.*, 2009, **38**, 1330.
- J. J. Gu, D. H. Hu, W. N. Wang, Q. H. Zhang, Z. Meng, X. D. Jia and K. Xi, *Biosens. Bioelectron.*, 2015, **68**, 27.
- (a) G. M. Sheldrick, *SHELXL97*, Program for Crystal Structure Refinement, University of Göttingen, Göttingen, Germany, 1997; (b) G. M. Sheldrick, *SHELXS97*, Program for Crystal Structure Solution, University of Göttingen, Göttingen, Germany, 1997.
- (a) L. Chen, X. J. Sang, J. S. Li, C. H. Shan, W. L. Chen, Z. M. Su and E. B. Wang, *Inorg. Chem. Commun.*, 2014, **47**, 138; (b) S. Ito, P. Chen, M. K. Nazeeruddin, P. Liska, P. Péchy and M. Grätzel, *Prog. Photovolt: Res. Appl.*, 2007, **15**, 603.

Abstract

A di-vanadium-substituted Lindqvist-type polyoxometalate $[\text{Cu}(\text{C}_{12}\text{H}_8\text{N}_2)_2]_2[\text{V}_2\text{W}_4\text{O}_{19}]\cdot 4\text{H}_2\text{O}$ (**1**) was hydrothermally synthesized and characterized structurally by single crystal X-ray diffraction analysis. X-ray photoelectron spectroscopy and Energy disperse spectroscopy tests further prove the existence of vanadium. Ultraviolet photoelectron spectroscopy and Density Functional Theoretical studies indicate that the energy level of **1** matches well with the conduction band of the TiO_2 . Furthermore, considering the semiconductor-like nature of **1** and the introduction of transition metal element Cu synchronously extends the absorption to the visible region, which should also be beneficial to the photovoltaic device performance. **1**-doped TiO_2 composites (denoted as **1**@ TiO_2) have been successfully fabricated by a simple sol-gel method, which were introduced into the dye-sensitized solar cells (DSSCs) as co-sensitizers in N719-sensitized photoanodes by mixing **1**@ TiO_2 with P25 nanoparticles with different weight ratios to enhance the photoelectric conversion efficiency. The investigations show that the DSSC assembled with **1**@ TiO_2 /19P25 photoanode has the best performance and the overall improvement of the efficiency is 21.6% compared with pure P25. Furthermore, the electrochemical impedance spectroscopy and open-circuit voltage decay investigations show that the cosensitization of **1** and N719 can promote electron transfer and restrain charge recombinations in the DSSCs, resulting in the longer electron lifetime.